Energy 237 (2021) 121596

Contents lists available at ScienceDirect

Energy

journal homepage: www.elsevier.com/locate/energy

Equation-oriented methods for design optimization and performance analysis of radial inflow turbines

Brede A.L. Hagen [a, *], Roberto Agromayor [a], Petter Nekså [a, b]

[a] Department of Energy and Process Engineering, NTNU – Norwegian University of Science and Technology, Kolbjørn Hejes Vei 1B, NO-7491, Trondheim, Norway

[b] SINTEF Energy Research, Sem Sælands 11, NO-7465, Trondheim, Norway

ARTICLE INFO

Article history:
Received 22 January 2021
Received in revised form
10 June 2021
Accepted 23 July 2021
Available online 28 July 2021

Keywords:
Mean-line model
Gradient-based optimization
Choked flow
Organic Rankine cycle
Model validation

ABSTRACT

This paper presents methods for design optimization and performance analysis of radial inflow turbines. Both methods are formulated in an equation-oriented manner and involve a single mathematical problem that is solved by an efficient, gradient-based optimization algorithm. In addition, the comparison of the model output with experimental data showed that the underlying mean-line flow model accurately predicts the variation of mass flow rate and isentropic efficiency as a function of the pressure ratio, rotational speed, and nozzle throat area. Moreover, the capabilities of the proposed methods were demonstrated by carrying out the preliminary design and performance prediction of the radial inflow turbine of an organic Rankine cycle. The results indicate that the design optimization method converges to the global optimum solution, regardless of the start values for the independent variables. In addition, the performance maps generated by the performance analysis method are physically consistent and agree with general findings from experimental data reported in the open literature. Considering the accuracy, robustness and low computational cost of the proposed methods, they can be regarded as a powerful tool for the preliminary design and performance prediction of radial inflow turbines, either as a standalone component or as part of a larger system.

1. Introduction

The Rankine cycle using an organic working fluid, conventionally referred to as the Organic Rankine Cycle (ORC), is an attractive technology for power production from low-temperature heat sources [1]. The ORC is currently applied for power production from waste heat [2] and renewable energy sources such as biomass combustion [3], concentrated solar energy [4] and geothermal energy [5]. Despite these energy sources could provide a significant fraction of the world's power demand [6], the full potential of ORC power systems has not yet been realized because the specific investment cost of this technology is relatively high compared with that of conventional power plants based on the combustion of fossil fuels [7]. Therefore, a key factor to enable further utilization of the ORC technology, and thus facilitate a reduction of CO_2 emissions, is to increase its cost-effectiveness.

One way to achieve this in applications for which the heat source or sink characteristics vary with time is to account for the off-design performance of the system during the design phase. For instance, Capra and Martelli [8] demonstrated that a design optimization that takes into account the off-design performance of the Rankine cycle can significantly increase the cost-effectiveness of the system with respect to a conventional design approach that only accounts for the system performance at the nominal operating point. More specifically, Capra and Martelli [8] applied the two aforementioned methods to design a combined heat and power Rankine cycle and showed that the former resulted in up to 22 % higher annual profit than the latter [8].

In order to account for the off-design performance of the Rankine cycle during the design phase, it is necessary to resort to accurate performance prediction methods for each of its components. In this context, the expander model is of key importance because the performance of this component has a strong influence on the mass flow rate and efficiency of the system. The importance of the expander efficiency prediction for ORC design optimization is illustrated by Song et al. [9], who performed two separate working fluid screening analyses; one using a prescribed expander efficiency and the other using a mean-line turbine model to predict the

* Corresponding author.
E-mail address: brede.hagen@ntnu.no (B.A.L. Hagen).

https://doi.org/10.1016/j.energy.2021.121596

Nomenclature

Latin symbols

a	Speed of sound [m/s]
A	Cross sectional flow area [m^2]
b	Blade height [m]
c	Blade chord length [m]
C	Absolute velocity [m/s]
C_0	Spouting velocity [m/s]
c_i	Rankine cycle state points
h	Specific enthalpy [J/kg]
k	Ratio of specific heat capacities [−]
$K_{p1}, K_{p2}, K_{p3}, K_{in}$	Loss model calibration coefficients [−]
L_z	Rotor axial length [m]
Ma	Relative Mach number, $Ma = W/a$ [−]
o	Throat opening [m]
p	Pressure [Pa]
r	Radial distance from shaft [m]
s	Specific entropy [J/kg K], Blade pitch [m]
t	Blade thickness [m]
U	Rotational velocity [m/s]
W	Relative velocity [m/s]
x_0	Independent variable − start value [−]
x_l	Independent variable − lower bound [−]
x_u	Independent variable − upper bound [−]
Z	Number of blades [−]

Greek symbols

α	Absolute flow angle [rad]
β	Relative flow angle [rad]
δ	Deviation angle [rad]
Δh	Specific work reduction due to loss [J/kg]
η	Total-to-static efficiency [−]
ε	Clearance [m]
ε	Convergence criterion [−]
ν	Velocity ratio [−]
μ	Dynamic viscosity [Pa s]
ρ	Density [kg/m^3]
ω	Rotational speed [rad/s]

Subscripts

0	Total state
1−6	RIT expansion state points
b	Blade
cl	Clearance loss
corr	Corrected
d	Design value
df	Disc friction loss
h	Hub
i	Incidence loss; State point index
int	Interspace loss
l	Loss
m	Meridional direction
n	Nozzle
opt	Optimal
out	Outlet of a blade row
p	Passage loss
r	Rotor
ref	Reference
s	Shroud; Specific
su	Supersonic loss
t	Tangential direction
te	Trailing edge loss
th	Throat of a blade row

Abbreviations

KKT	Kerush Kuhn Tucker
ORC	Organic Rankine Cycle
RIT	Radial Inflow Turbine
RMS	Root mean square

expander efficiency at its design point. Their results showed that the inclusion of the mean-line model can change the optimal working fluid in terms of net power output and that the predicted expander efficiency can differ up to 11% points among the working fluids considered. Expander performance prediction is arguably even more important for off-design analyses because both the expander efficiency and mass flow rate can change when the operating conditions are modified. As an example of this, Chatzpoulou et al. [10] performed off-design analyses of an ORC converting heat from an internal combustion engine into power. They considered a constant expander efficiency and a variable efficiency predicted by a piston expander model, and they found that the analyses that assumed a constant expander efficiency led to a net power underestimation of up to 17 %.

Among the different architectures available for ORC expanders, the Radial Inflow Turbine (RIT) is particularly promising thanks to its high-compactness and its capability to accommodate a large pressure ratio in a single stage [11]. In addition, the RIT can be equipped with movable nozzle blades, known as variable guide vanes, that can modify the nozzle throat area and the nozzle exit flow angle by rotating around a pivot point [12,13]. As a result, variable-geometry RITs offer more flexibility during off-design operation than fixed-geometry turbines [14].

From the point of view of a Rankine cycle system analysis, using a mean-line flow model to predict the performance of a RIT can be regarded as a satisfactory compromise between model complexity and prediction accuracy. A selection of RIT mean-line models developed for Rankine cycle applications and documented in the open literature is summarized in Table 1. The methods differ on whether they can be applied for design optimization, performance analysis, or both. In addition, some of the methods considered RITs with movable nozzle blades, whereas most of them are limited to fixed-geometry turbines. Moreover, the mean-line models also differ with respect to which loss mechanisms are included. In particular, the losses associated with supersonic flow conditions in the nozzle or rotor blade rows, such as shock waves and intense mixing, are especially relevant in Rankine cycle turbines due to the potential combination of high-pressure ratio and low speed of sound of the working fluid. However, only a limited number of RIT mean-line models account for these complicated loss mechanisms and, to the knowledge of the authors, the only correlations available in the open literature are simple functions of the Mach number whose generality and accuracy could be questioned [15,16](p. 82).

As seen in Table 1, most of the RIT mean-line models documented in the open literature have been validated against experimental data or CFD simulations. In most cases, the model validation only considered data from one turbine operating at its design pressure ratio. Indeed, the model predictions from Refs. [17,23,24] showed a good agreement with the experimental data by Jones [27] at the design pressure ratio of 5.7. However, these authors did not

Table 1
Selection of RIT mean-line models applied for Rankine cycle analyses in the open literature.

Reference		Variable geometry	Design optimization/Performance analysis	Supersonic loss mechanisms	Validation
Hu et al. (2015)	[17]	No	Both	No	Exp.
Demierre et al. (2015)	[18]	No	Performance analysis	No	Exp.
Song et al. (2016)	[19]	No	Both	No	No
Da Lio et al. (2017)	[20]	No	Design optimization	Yes	No
Meroni et al. (2018)	[21]	No	Both	Yes	Exp./CFD
Alshammari et al. (2018)	[22]	No	Performance analysis	No	Exp.
Du et al. (2019)	[23]	Yes	Both	No	Exp
Liu and Gao (2019)	[24]	Yes	Both	No	Exp
Zhou et al. (2020)	[25]	No	Design optimization	No	CFD
Schuster et al. (2020)	[14]	Yes	Both	No	Exp.
Lee et al. (2021)	[26]	No	Performance analysis	No	CFD
Present work		Yes	Both	Yes	Exp.

present a comparison between experimental data and model predictions for the other 7 pressure ratios reported in Ref. [27]. Therefore, the accuracy of their models for off-design operation at other pressure ratios or for other turbine geometries is unknown.

The mean-line model presented by Meroni et al. [21] is arguably the most accurate for high-pressure ratio applications. The reason for this is twofold. First, the loss model that they adopted considers various loss mechanisms occurring in the nozzle and the rotor blade rows, including supersonic losses that are present when the flow velocity exceeds the speed of sound. Secondly, they calibrated some of the fitting constants of the loss model to minimize the deviation between the experimental data from six high pressure-ratio RITs and the corresponding model predictions. However, the performance prediction method proposed by Meroni et al. [21] requires an a priori numerical solution strategy to identify the choked nozzle mass flow rate, which is followed by an evaluation of whether the nozzle or the rotor chokes first as the pressure ratio increases. The remaining calculation procedure depends on the results from the initial analysis and it involves the solution of several systems of nonlinear equations. Although their method appears suitable for generating RIT performance maps, Meroni et al. [21] did not report the execution time required to compute each operating point and, therefore, it is not clear if their method is suitable for system-level analyses.

In fact, the robustness and computational cost of the methods for RIT design optimization and performance analysis documented in the open literature is overlooked in the majority of cases. As a notable exception, Hagen et al. [28] proposed an equation-oriented RIT design optimization method and applied it to a case study to show that the optimization problem is well-behaved and that the design optimization reliably converged to the global optimum in about 1 s.

Considering the limitations of the methods surveyed in Table 1, the aim of the present paper is to extend the work presented in Hagen et al. [28] and document the development of two robust and computationally efficient methods for the design optimization and performance analysis of RITs. The methods proposed in this work are based on a mean-line flow model and contain the following novel aspects: (1) the design optimization method uses a gradient-based optimization algorithm and relies on equality constraints to search for the optimal solution and close the model equations; (2) the performance prediction method uses a new numerical treatment of flow choking that is valid for subsonic and supersonic conditions and does not require an a priori solution strategy to identify whether the nozzle or the rotor are choked; and (3) each of the methods only requires the solution of a single mathematical problem, namely, a constrained optimization problem (design optimization) or a system of nonlinear equations (performance analysis).

The paper is organized as follows. The mean-line model and the mathematical formulation of the design optimization and performance analysis methods are described in Sec. 2. After that, the experimental data by Jones [27] and Spence et al. [29,30] are used to validate the mean-line flow model in Sec. 3. Finally, the capabilities of the proposed methods are demonstrated in Sec. 4 through a case study. First, a preliminary design for a RIT for an ORC power system is obtained using the design optimization method. Thereafter the RIT performance analysis method is applied to predict the performance maps of the designed turbine for various rotational speeds and nozzle throat areas. The conclusions drawn from this study are summarized in Sec. 5.

2. Methodology

The proposed methods for RIT design optimization and performance analysis consist of a problem formulation, a mean-line flow model and a gradient-based optimization algorithm. The illustration of the methods shown in Fig. 1 is valid for both design optimization and performance analysis.

The main difference between the two methods is the *problem formulation* step, where the RIT parameters are divided into three categories:

1. The *fixed parameters* are predefined by the user and do not change during the simulation. The RIT inlet state and outlet pressure are examples of fixed parameters in both the design optimization and performance analysis.
2. The *independent variables* are adjusted by the optimization algorithm to find the numerical values that optimize a certain objective function subject to constraints.
3. The *dependent variables* are computed using the independent variables and fixed parameters and they include the objective function and constraints.

A major part in the development of the problem formulation is grouping the RIT parameters into the three above-mentioned parameter categories and defining corresponding constraints and an objective function. A detailed presentation of methods for design optimization and performance analysis is presented in the following two subsections.

2.1. Design optimization

The problem formulation for RIT design optimization is shown in Table 2 (independent variables, constraints and objective function) and Table 3 (fixed and dependent RIT geometry variables). The optimization objective is to maximize the total-to-static isentropic efficiency. This objective function was selected because it is

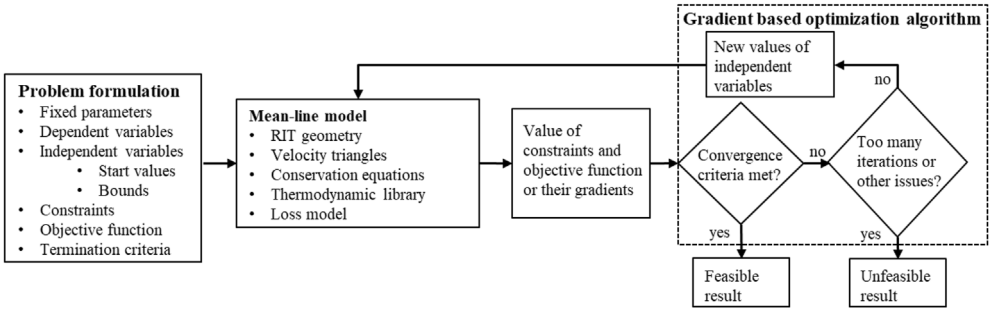

Fig. 1. Overview of the proposed methods for RIT-design optimization and performance analysis.

Table 2
Independent variables, constraints and objective function for design optimization.

Description	Symbol/formula	x_l	x_0	x_u
Nozzle outlet velocity	C_2/C_0	0.1	0.7	0.9
Nozzle outlet flow angle	α_3	40°	60°	80°
Rotor inlet meridional velocity	C_{4m}/C_0	0.02	0.20	0.40
Rotor outlet velocity	W_6/C_0	0.1	0.3	0.9
Rotor outlet flow angle	β_6	−70°	−68.5°	−20°
Specific speed	$\omega_s = \omega\dot{V}_{6,is}^{1/2}/\Delta h_{is}^{3/4}$	0.2	0.4	0.8
Velocity ratio	$\nu = U_4/c_0 = \omega r_4/C_0$	0.5	0.65	0.8
Rotor radius ratio (shroud/inlet)	r_{6s}/r_4	0.4	0.65	0.7
Rotor radius ratio (hub/shroud)	r_{6h}/r_{6s}	0.4	0.7	0.8
Blade height to radius ratio	b_3/r_4	0.04	0.1	0.34
Blade row outlet entropy[a,b]	s_{out}/s_1	1.0	1.0	s_{ref}/s_1
Constraints				
Consistent outlet pressure	$1.0 - p_6/p_{out} = 0$			
Consistent nozzle outlet enthalpy	$\frac{h_3 - h(p_3, s_{01}) - \sum_l \Delta h_{n,l}}{0.5C_3^2} = 0$			
Consistent rotor outlet enthalpy	$\frac{h_6 - h(p_6, s_4) - \Delta h_{int} - \sum_l \Delta h_{r,l}}{0.5W_6^2} = 0$			
Conservation of mass[c]	$1.0 - \rho WA\cos\beta/\dot{m} = 0$			
Minimum degree of reaction	$\frac{h_4 - h_6}{h_{01} - h_{06}} - 0.45 \geq 0$			
Objective function				
Maximize total-to-static efficiency	$\eta = \frac{h_{01} - h_{06}}{\Delta h_{is}}$			

[a] Two variables (nozzle and rotor).
[b] Reference entropy, s_{ref}, is the resulting outlet entropy when $\eta = 0.5$.
[c] Three constraints (nozzle outlet, rotor inlet and rotor outlet).

assumed that the kinetic energy leaving the rotor outlet is not recovered. The independent variables that govern the geometry, flow and thermodynamic parameters include both engineering decision variables, such as specific speed and velocity ratio, and parameters that are unknown a priori, such as the entropy distribution. The upper and lower bounds used to constrain the independent variables, as well as typical start values, are indicated in Table 2. The bounds on the independent RIT geometry and flow angle variables were set in accordance with the limits suggested in Refs. [16,17,31]. More specifically, this work applies the most conservative values from the above-mentioned references to ensure a feasible design. The normalized velocity variables cannot, due to conservation of energy, exceed the range between 0 and 1. However, a slightly smaller range of those variable were applied to limit the domain of the design space. In addition, the bounds for the specific speed and velocity are based on the results obtained by Da

Table 3
Value of fixed parameters and formulas of the dependent RIT geometry variables for design optimization.

Parameter	Symbol	Value	Source
Nozzle blade trailing edge thickness	t_3	$0.012c_n$	[16] (p. 256)
Rotor blade trailing edge thickness	t_6	$0.02r_4$	[16] (p. 240)
Rotor axial length	L_z	$1.5(r_{6s} - r_{6h})$	[16] (p. 240)
Blade tip clearances	$\varepsilon_a, \varepsilon_r$	0.4 mm	[33]
Disc clearance	ε_d/r_4	0.05	
Nozzle chord to pitch ratio	c_n/s_3	1.33	[16](p. 256)
Interspace distance	$r_3 - r_4$	$2b_3\cos\alpha_3$	[16](p. 256)
Number or rotor blades	Z_r	$12 + 0.03(\alpha_3 - 57°)^2$	[16,32], (p. 240)
Number of nozzle blades	Z_n	$Z_r + 3$	
Blade height, rotor inlet	b_4	b_3	

Lio et al. [20], who found that the maximum efficiency predicted by their model occurs when the specific speed is around 0.4 and the velocity ratio is in the range of 0.6–0.7.

When formulating the design problem, it was realized that some RIT geometry parameters are not suitable for optimization. For instance, the number of blades and the nozzle chord to pitch ratio always reached either their lower or upper bounds during initial design optimization tests. Consequently, fixing these parameters to the value of their active bound reduces the complexity of the mathematical problem without affecting the outcome of the optimization. In addition, other parameters, such as blade edge thicknesses and rotor tip clearances, are constrained due to factors not included in the model (e.g., manufacturing requirements or stress considerations).

Consequently, all these parameters are either fixed or calculated from the set of independent variables during the optimization. The value of the fixed parameters and formulas for the dependent RIT geometry variables are shown in Table 3, and most of these were suggested default values from Aungier [16]. The empirical formula used to compute the number of rotor blades was developed by Rohlik [32] and recommended by Aungier [16]. Several scientific works report or assume rotor blade tip clearances, ε_a, ε_r, in the range 0.21–0.50 mm [14,20,27,29,31]. However, extensive development of small gas turbines have shown that it is difficult to maintain clearances less than about 0.4 mm [33,34](p. 354). For this reason, a conservative value of 0.4 mm is assumed for the rotor tip clearances. Finally, the disc clearance and the number or nozzle blades were assigned arbitrary, yet realistic, values. The influence of these two variables on the design efficiency is negligible in comparison to that of other parameters, as demonstrated in the sensitivity analysis shown in Fig. 9.

The design optimization starts by computing the isentropic enthalpy change, $\Delta h_{is} = h_{01} - h(p_{out}, s_{01})$, using the prescribed inlet state and outlet pressure. This enables the calculation of the spouting velocity, $C_0 = \sqrt{2\Delta h_{is}}$. Thereafter the rotational speed and the rotor inlet radius can be computed from the independent specific speed and velocity ratio variables. After that, the remaining geometry parameters can be calculated using the independent geometry variables and the fixed- and dependent geometry parameters. The geometry parameters involved in the mean-line model are illustrated in Fig. 2.

Once the RIT geometry is described, the dependent variables required to evaluate the objective function and constraints are computed by means of the mean-line model. This model assumes that the flow is uniform along the blade span and evaluates the velocity triangles and thermophysical properties at the inlet, throat, and outlet of the nozzle and rotor blade rows, see Fig. 2. As usually done in the context of mean-line modelling [14,21], the presence of boundary layers near the surfaces of the blades, hub, and shroud was neglected. Consequently, the mass flow rate constraints of Table 2 were evaluated using the geometrical cross-section area given by Eqs. (1) and (2).

$$A_i = 2\pi r_i b_i, \quad i = 3, 4 \tag{1}$$

$$A_6 = \pi\left(r_{6s}^2 - r_{6h}^2\right) \tag{2}$$

The mean-line model starts by computing the nozzle outlet enthalpy by conservation of energy, Eq. (3).

$$h_3 = h_{01} - \frac{1}{2}C_3^2 \tag{3}$$

The enthalpy and velocity at the inlet of the rotor are calculated by conservation of angular momentum, Eq. (4), and energy, Eq. (5), through the interspace.

$$C_{4t} = \frac{r_3}{r_4}C_{3t} \tag{4}$$

$$h_4 = h_{01} - \frac{1}{2}\left(C_{4m}^2 + C_{4t}^2\right) = h_{01} - \frac{1}{2}C_4^2 \tag{5}$$

The rotor outlet enthalpy is then calculated by conservation of rothalpy through the rotor, Eq. (6).

$$h_6 = h_4 + \frac{1}{2}\left(W_4^2 - U_4^2\right) - \frac{1}{2}\left(W_6^2 - U_6^2\right) \tag{6}$$

A simplification is performed regarding the computation of the thermodynamic state and velocity at the throat of the blade rows (state points 2 and 5). Namely, the thermodynamic state at the throat is assumed to be equal to the blade row outlet state and the relative velocity at the throat is computed according to Eq. (7).

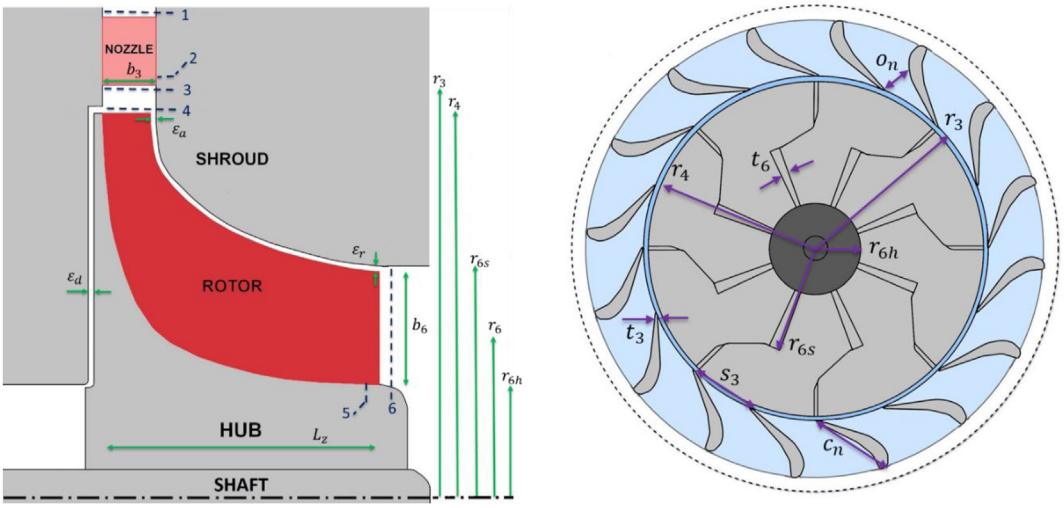

a) View at the meridional plane **b) View in the axial direction**

Fig. 2. Illustration of the radial inflow turbine and the geometry parameters involved in the mean-line model.

$$W_{th} = \begin{cases} W_{out}, \ Ma_{out} < 1 \\ a(h_{out}, s_{out}), \ Ma_{out} \geq 1 \end{cases} \tag{7}$$

The thermodynamic states except the inlet state are defined by enthalpy and entropy. The remaining relevant thermophysical properties in these states are calculated by enthalpy-entropy function calls, Eq. (8).

$$\rho_i, \ T_i, \ p_i, \ \mu_i, a_i = f(h_i, s_i), \ i = \{2, 6\} \tag{8}$$

The mean-line model is compatible with any thermodynamic library that supports enthalpy-entropy function calls. In this work, the thermodynamic calculations were performed using REFPROP v10.0 [35].

Furthermore, the losses due to irreversibilities within the turbine are estimated using an empirical loss model. The loss model adopted in this work, Table 4, was proposed by Meroni et al. [21] and considers loss mechanisms in the nozzle, interspace and the rotor, including the losses related to supersonic flow conditions.

The coefficients K_{in}, K_{p1}, K_{p2} and K_{p3} were introduced by Meroni et al. [21] to calibrate the loss model. More specifically, they adjusted the calibration coefficients by means of a genetic algorithm with the aim to minimize the average root mean square (RMS) deviation between experimental data from six high-pressure ratio RITs and corresponding model predictions. The model validation presented in this work consider both the original- and the calibrated loss model defined in Table 5. A more complete account of the equations and parameters involved in the loss model is presented in Appendix A.

Table 5
Values of the calibration coefficients in the loss models [21].

	Calibrated loss model	Original loss model
K_{p1}	1.3881	1.0
K_{p2}	0.6370	1.0
K_{p3}	0.1042	1.0
K_{in}	0.8952	1.0

The proposed design strategy takes advantage of equality constraints to ensure that the mathematical model is consistent. For example, two equality constraints are imposed to ensure that the calculated enthalpy distribution is consistent with the predicted enthalpy losses and three equality constraints are imposed to ensure that the mass flow rate is conserved and its value is equal to the design specification. In addition, other equality- or inequality constraints may be readily imposed to ensure that the outcome of

Table 4
Summary of the loss model from Meroni et al. [21] that is applied in this work.

Mechanism	Correlation	
Nozzle passage[a]	$\Delta h_{n,p} = K_{p1} \frac{0.05}{Re_2^{0.2}} \left[\frac{3 \tan \alpha_2}{s_3/c_n} + \frac{s_3 \cos \alpha_2}{b_3} \right] \frac{1}{2} C_2^2$	(9)
Nozzle trailing edge[a]	$\Delta h_{n,te} = \left(\frac{t_3}{s_3 \cos \alpha_2} \right)^2 \frac{1}{2} C_2^2 Y_2$	(10)
Nozzle supersonic	$\Delta h_{n,su} = \left(\frac{M_3 - M_2}{M_3} \right)^2 \frac{1}{2} C_3^2 Y_3$	(11)
Interspace	$\Delta h_{int} = C_f \frac{L}{D} \frac{1}{2} \left(\frac{C_3 + C_4}{2} \right)^2$	(12)
Rotor incidence	$\Delta h_{r,i} = K_{in} \frac{1}{2} W_4^2 \sin^2 (\beta_4 - \beta_{4,opt})$	(13)
Rotor passage[a]	$\Delta h_{r,p} = 0.11 \left\{ K_{p2} \frac{L_H}{D_H} + 0.68 K_{p3} \left[1 - \left(\frac{r_6}{r_4} \right)^2 \right] \frac{\cos \beta_{6b}}{b_6/c_r} \right\} \frac{1}{2} \left(W_4^2 + W_5^2 \right)$	(14)
Rotor trailing edge[a]	$\Delta h_{r,te} = \left(\frac{Z_r t_6}{\pi (r_{6s} + r_{6h}) \cos \beta_5} \right)^2 \frac{1}{2} W_5^2 Y_5$	(15)
Rotor clearance	$\Delta h_{r,cl} = \frac{U_4^3 Z_r}{8\pi} \left\{ 0.4 \varepsilon_a K_a + 0.75 \varepsilon_r K_r - 0.3 \sqrt{\varepsilon_a \varepsilon_r K_a K_r} \right\}$	(16)
Rotor disc friction[a]	$\Delta h_{r,df} = 0.25 K_f \frac{\rho_4 + \rho_5}{2} \frac{U_4^3 r_4^2}{\dot{m}}$	(17)
Rotor supersonic	$\Delta h_{r,su} = \left(\frac{M_6 - M_5}{M_6} \right)^2 \frac{1}{2} W_6^2 Y_6$	(18)

[a] The point indices corresponding to the blade row throat states (points 2 or 5) do not match with the indices stated in Ref. [21] who, instead, adopted the blade row outlet states (points 3 or 6). However, a personal communication with Andrea Meroni confirmed that Ref. [21] actually used the throat velocity (and not the row outlet velocity) to compute the passage- and trailing edge losses because they believed it to be the most consistent way to express the losses.

the optimization satisfies additional design requirements such as a given degree of reaction or a maximum rotational speed.

The gradient-based algorithm applied in this work was NLPQL [36], which is a sequential quadratic programming (SQP) method that can be applied for solving both constrained optimization problems and systems of nonlinear equations. Gradients are calculated using a second order central difference approximation for numerical differentiation. The step length used to perturb the independent variables during the gradient estimation is shown in Table 6 and is approximately three orders of magnitude smaller than the value of the independent variables. The Kerush Kuhn Tucker (KKT) optimal criterion is set to 1.0E-7 and the maximum number of iterations is set to 80. This means that NLPQL returns an unfeasible result if the KKT optimal criterion is not met within 80 iterations or other issues occur, see Ref. [36] for details.

2.2. Performance analysis

The independent variables and constraints for the RIT performance analysis are summarized in Table 7. The independent variables include the unknown velocities and entropy distribution, and several equality constraints are imposed to ensure internal consistency. The number of independent variables equals the number of equality constraints, meaning that there are zero degrees of freedom for optimization and the mathematical problem is a system of nonlinear equations.

The calculation procedure for performance analysis is very similar to that for design optimization. However, in the performance analysis method, the RIT geometry and rotational speed are defined as fixed parameters. In addition, instead of being independent variables, the blade row outlet flow angles are calculated using the throat area and the equation of conservation of mass as indicated in Fig. 3. The only inner iteration in the mean-line model activates when outlet velocity of a blade row is supersonic. In such case, the throat velocity is first guessed as the speed of sound at the outlet. Thereafter multiple successive substitutions are performed until the throat Mach number converges to 1.0. A relatively strict convergency criterion ($\varepsilon = 10^{-10}$) is set to ensure accurate numerical gradient estimations. In the case of subsonic outlet velocity, no iteration is required to compute the thermodynamic state at the throat. Instead, the thermodynamic state at the throat and outlet are assumed to be equal. In this case, the formula for computing the outlet flow angle becomes equivalent to the well-known cosine rule since the density and velocity factors cancel each other out.

In contrast with the design optimization formulation, the performance analysis also uses the entropy at the throat of each blade row as independent variables. The reason for this additional complexity is to ensure physically consistent results in the case when the flow in either of the blade rows is choked. A reliable RIT performance analysis should predict a mass flow rate that increases with pressure ratio (by reducing the outlet pressure) until it converges to a limiting value that corresponds to the case when the flow velocity in either of the blade rows reaches the speed of sound. At this point the blade row is choked and a further increased pressure ratio will not affect the mass flow rate, or the thermodynamic states and velocity triangles upstream of the throat [37] (p. 264–265) The additional entropy variables and corresponding constraints ensure that, once a blade row is choked, a further increase in pressure ratio will not affect the thermodynamic state at the throat or any points upstream of the throat. Instead the additional entropy production due to supersonic losses is assigned at the outlet of the blade row. Thus, the mass flow rate, which depends on the density at the throat, will remain constant beyond the choking point.

Table 6
Step lengths for numerical differentiation used in the model validation and the case study.

Independent variable	Step length for numerical differentiation
$C_3/\ c_0$, $C_{4m}/\ c_0$, $W_6/\ c_0$	10^{-3}
ω_s	
ν, $r_{6s}/\ r_4$, $r_{6h}/\ r_{6s}$	
$b_3/\ r_4$	10^{-4}
α_3, β_6	10^{-3} rad
Entropy variables	$(1 - s_{ref}/s_{01})\cdot 10^{-3}$

2.3. Model implementation and compilation

The mean-line model, problem formulations and interfaces with the Fortran source code of the optimization algorithm and the thermodynamic library are written in the C programming language. The executable files for running the design optimization and performance analysis were built using the GNU [38] compilers *gcc* and *gfortran*.

2.4. Discussion of the problem formulations

Developing a simple and effective problem formulation is a challenging task that requires creativity and a solid understanding of the underlying mathematical models and the numerical algorithms used to solve the problem. We believe that the proposed design optimization and performance analysis problem formulations have some advantages that are worth highlighting:

1. The independent variables, constraints and the objective function are written in non-dimensional form. For instance, the velocity variables are scaled by the spouting velocity and the angular variables are converted to radians. A non-dimensional problem formulation is not only advantageous from a numerical point of view, but it is also advantageous from a practical standpoint because the initial guess and bounds of the independent variables can be defined using physical principles and general design guidelines instead of being tailored to each specific application.
2. The use of a predefined outlet pressure in the performance analysis ensures a unique solution of the problem. In the case of predefined mass flow rate (as in Schuster et al. [14] and Meroni et al. [21]), care must be taken to specify a problem with a unique and feasible solution. This is because, once the flow is choked, there is an infinite number of values for the outlet pressure that yield the same mass flow rate, see Fig. 11. Schuster et al. avoided numerical problems by considering subsonic turbines only, while the approach in Ref. [21] involved use of a numerical method to detect the choked mass flow rate. In addition, in the case of a choked turbine, Meroni et al. [21] provided a predefined outlet pressure together with the mass flow rate to ensure a unique solution.
3. The use of blade row outlet velocities as independent variables avoids the need for an a priori numerical solution strategy for identifying whether any blade rows are choked as in Meroni et al. [21]. Instead, the choked flow calculation activates every time the blade row outlet flow velocity is supersonic. However, whether the blade row actually chokes depends solely on the magnitude of the outlet Mach number at the last iteration before a feasible solution is found.
4. In contrast with other published methods, see Table 1, the equation-oriented formulation of the design optimization avoids the use of inner iterations. Instead, the model equations

Table 7
Independent variables and constraints for performance analysis.

Description	Symbol
Nozzle outlet velocity	C_3/c_0
Rotor inlet meridional velocity	C_{4m}/c_0
Rotor outlet velocity	W_6/c_0
Blade row throat entropy[a]	s_{th}/s_{01}
Blade row outlet entropy[a]	s_{out}/s_{01}
Constraints	
Consistent outlet pressure	$1.0 - p_6/p_{out} = 0$
Consistent nozzle throat enthalpy	$\frac{h_2 - h(p_2, s_{01}) - \sum_{l \neq su} \Delta h_{n,l}}{0.5C_3^2} = 0$
Consistent nozzle outlet enthalpy	$\frac{h_3 - h(p_3, s_{01}) - \sum_{l} \Delta h_{n,l}}{0.5C_3^2} = 0$
Consistent rotor throat enthalpy	$\frac{h_5 - h(p_5, s_4) - \Delta h_{int} - \sum_{l \neq su} \Delta h_{r,l}}{0.5W_6^2} = 0$
Consistent rotor outlet enthalpy	$\frac{h_6 - h(p_6, s_4) - \Delta h_{int} - \sum_{l} \Delta h_{r,l}}{0.5W_6^2} = 0$
Conservation of mass[b]	$1.0 - \rho W A \cos\beta / \rho_3 C_3 A_3 \cos\alpha_3 = 0$

[a] Two variables (nozzle and rotor).
[b] Two constraints (Rotor inlet and rotor outlet).

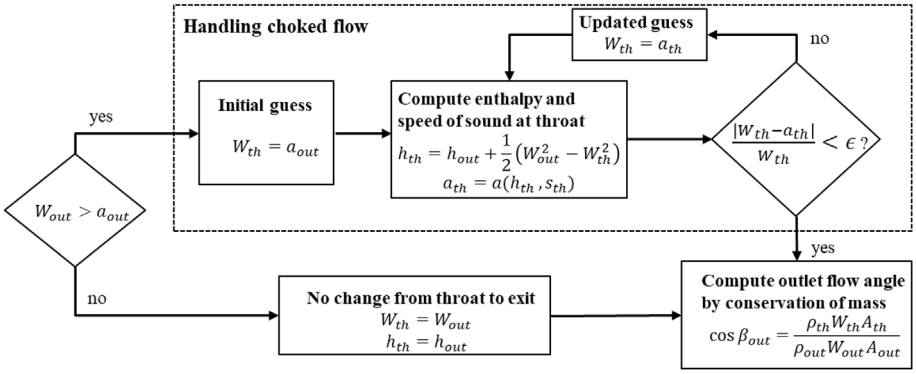

Fig. 3. Method used to compute the velocity and thermodynamic state at the throat and the outlet flow angle of a blade row in the performance analysis method.

are closed by means of equality constraints that are processed at once by the gradient-based optimization algorithm. As a result, the model equations do not have to be converged at each optimization iteration and the computational cost of the problem is reduced.

5. The optimization algorithm used in the performance analysis method could be replaced by a nonlinear equation solver because the number of equality constraints equals the number of independent variables. However, using the same algorithm for design optimization and performance analysis yields a smooth transition between the two methods. In addition, the optimization algorithm gives the additional flexibility of formulating the performance analysis as an optimization problem. For instance, little additional effort is required to modify the proposed performance analysis method to automatically find the rotational speed that maximizes the off-design efficiency.

3. Model validation

Several sets of experimental RIT data have been published in the open literature, but only a few of them are of sufficient quality to be applied for model validation [39]. A high-quality set of experimental data should contain measurements taken at different pressure ratios and rotational speeds. In addition, the RIT geometry should be documented such that it can be replicated within the

Table 8
RIT operating conditions and geometry for model validation.

			Spence et al. [29,30]	Jones [27]
Operating conditions	Fluid		Air	Air
	p_{01}	[bar]	1.3–3.6	4.136
	T_{01}	[°C]	126.85	204.45
	p_{out}	[bar]	1.01325	0.44–1.36
Nozzle	r_3	[mm]	55.5	63.5
	b_3	[mm]	10.2	6.0
	Z_n	[−]	16	19
	A_2	[mm^2]	653–1387[b]	491
	t_3	[mm]	1.0	0.51
	c_n	[mm]	37.4	22.9
Rotor	ω	[RPM]	30000–60000[a]	56000–83000
	r_4	[mm]	49.5	58.2
	r_{6s}	[mm]	39.5	36.8
	r_{6h}	[mm]	15.0	15.2
	b_4	[mm]	10.2	6.35
	Z_r	[−]	11	16
	t_6	[mm]	1.60	0.76
	A_5	[mm^2]	2317	1910
	L_z	[mm]	41.0	38.9
	c_r	[mm]	47.8[c]	45.7
	ε_a	[mm]	0.40	0.40
	ε_r	[mm]	0.40	0.21
	ε_d	[mm]	0.25	0.33

[a] Corrected speed, $\omega_{corr} = \omega\sqrt{T_{01}/T_{ref}}$, $T_{ref} = 288$ K.
[b] Computed as $A_2 = Z_n b_3 o_n$.
[c] Computed by Eq. (A.6) using $\beta_{6b} = -50.1°$.

mean-line model. In this work, the proposed mean-line model was validated against two comprehensive data sets whose geometric parameters and operating conditions are listed in Table 8. The reader is referred to Refs. [12,17] for an overview of other experimental data sets that could be used for RIT mean-line model validation.

3.1. Experimental data

The first data set is by Spence et al. [29,30], who performed experiments on 10 different turbine configurations. All cases consisted of the same rotor surrounded by a ring of nozzle blades operating at different setting angles. Consequently, the geometric characteristics of the turbines only differ in nozzle throat opening [29,30]. Hence, this data set is ideal for validating a variable-geometry RIT model. To the best of our knowledge, the experimental data of Spence et al. has rarely been used for model validation. The only study found in which data from Ref. [29] were used for model validation was Ref. [22]. However, only data for the turbine with the smallest nozzle throat opening was considered in that study. The experimental data from Spence et al. covers efficiency and corrected mass flow rate measured at different pressure ratios and rotational speeds. To facilitate comparison of predicted mass flow rates with experimental data, the corrected mass flow rate was calculated by Eq. (19). The reference pressure and temperature were set to standard atmospheric conditions in accordance with Ref. [29].

$$\dot{m}_{corr} = \dot{m}\sqrt{T_{01}/T_{ref}}\cdot p_{ref}/p_{01} \tag{19}$$

The second data set is by Jones [27], who performed measurements at 8 different pressure ratios, ranging from 3 to 9. Hence, this data set is ideal for validating a RIT mean-line models for high-pressure ratio applications, such as Rankine cycle power systems. Data from Ref. [27] has been widely used for model validation after it was rediscovered by Sauret [39], who also published more geometry information regarding Jones' turbine. However, to the best of our knowledge, only the data at the design pressure ratio of 5.7 have previously been used for model validation. The turbine analyzed by Jones had an exhaust diffuser to recover some of the kinetic energy leaving the rotor. In order to account for this, we modeled the diffuser with a fixed recovery coefficient, $c_d = 0.55$, (value given in Ref. [27]). This means that the computed rotor outlet pressure had to be replaced by the diffuser outlet pressure in the equality constraint used to ensure a consistent outlet pressure, see Table 7.

3.2. Results

A qualitative comparison of experimental data from three of the turbines from Spence et al. [29,30] and the corresponding mean-line model predictions with the original and calibrated loss models, as defined in Table 5, is shown in Fig. 4. As seen in Fig. 4(b,d,f), the mean-line model slightly overpredicts the mass flow rate in both cases. Part of this overprediction could be attributed to the neglection of boundary layer effects. Indeed, an approximate flat-plate boundary layer analysis indicated that the combined displacement thickness in the nozzles might be about 2−3% of the throat opening. The loss model also affects the predicted mass flow rate illustrated by the larger mass flow rates predicted by the calibrated loss model. In any case, the mean-line model is able to predict that the mass flow rate increases with increasing pressure ratio, decreasing rotational speed, and increasing nozzle throat opening, which agrees with the experimental data. Concerning the efficiency, Fig. 4(a,c,e), the mean-line model generally overestimates its value except for some pressure ratios at the lowest rotational speed. Despite this, the model captures the main trends; the rotational speed has a strong effect on the efficiency and lower rotational speeds yield better efficiency at lower pressure ratios and vice versa. In addition, the pressure ratio in which the peak efficiency occurs is predicted reasonably well for different rotational speeds and nozzle throat openings. Moreover, it can be observed that the predictions obtained using the calibrated loss model deviate more from the experimental data in Fig. 4 than those obtained using the original loss model.

A comparison of experimental efficiency data from Jones [27] and corresponding model predictions are shown in Fig. 5. Each plot (a,b,c,d) represents data at a single pressure ratio and the x-axis corresponds different rotational speeds expressed as the velocity ratio. The calibrated loss model predicts a higher efficiency than the original loss model in all cases. In addition, the original loss model agrees better with the experimental data at the lower pressure ratios, while the calibrated loss model agrees better with the experimental data at the larger pressure ratios. Moreover, both loss models predict the velocity ratio in which the peak efficiency occurs to be around 0.7. This agrees quite well with the experimental data at pressure ratio of 4.0, see Fig. 5(a). However, at larger pressure ratios, the experimental data indicates that the maximum efficiency is achieved at a slightly higher velocity ratio (about 0.75).

Figs. 4 and 5 only represent a fraction of the experimental data from the 10 turbine configurations in Spence et al. [29,30] and the 8 pressure ratios in Jones [27]. Nonetheless, the trends observed in these figures also hold for the remaining test conditions and they were not plotted for the sake of brevity. Instead, the Root Mean Square (RMS) deviation between experimental data and model prediction in terms of mass flow rate and isentropic efficiency was computed for all test conditions and summarized in Table 9. The results indicate that the original loss model, on average, agrees better with the experimental data of Spence et al. [29,30] than the calibrated loss model does. However, this situation is reversed for the experimental data by Jones [27]. In this case, the calibrated loss model yields a lower RMS efficiency-deviation and predicts the design point mass flow rate with a deviation below one percent. The calibrated loss model was trained using data from high-pressure ratio RITs and it is not surprising that it is more accurate than the original loss model for such cases.

4. Case study

In this section the proposed design optimization and performance analysis methods were applied to design and analyze a RIT for the transcritical ORC considered in Ref. [40], see Fig. 7. As the design pressure ratio for this case study is relatively low (4.87), the calculations were carried out using the more conservative *original* loss model.

4.1. Design optimization

The design optimization was performed using the problem formulation from Tables 2 and 3 and the operation conditions indicated in Fig. 6. The main results obtained from the design optimization are summarized in Table 10. The values of the specific speed and velocity ratio agree well with the values reported by Da Lio et al. [20]. The design optimization performed by Hu et al. [17] obtained almost the same specific speed (0.42) as in this work, but a slightly larger velocity ratio (0.7). Moreover, two independent RIT geometry variables had an active variable bound. Namely, the ratio r_{6s}/r_4 reached its upper bound of 0.7 and the ratio b_3/r_4 reached its

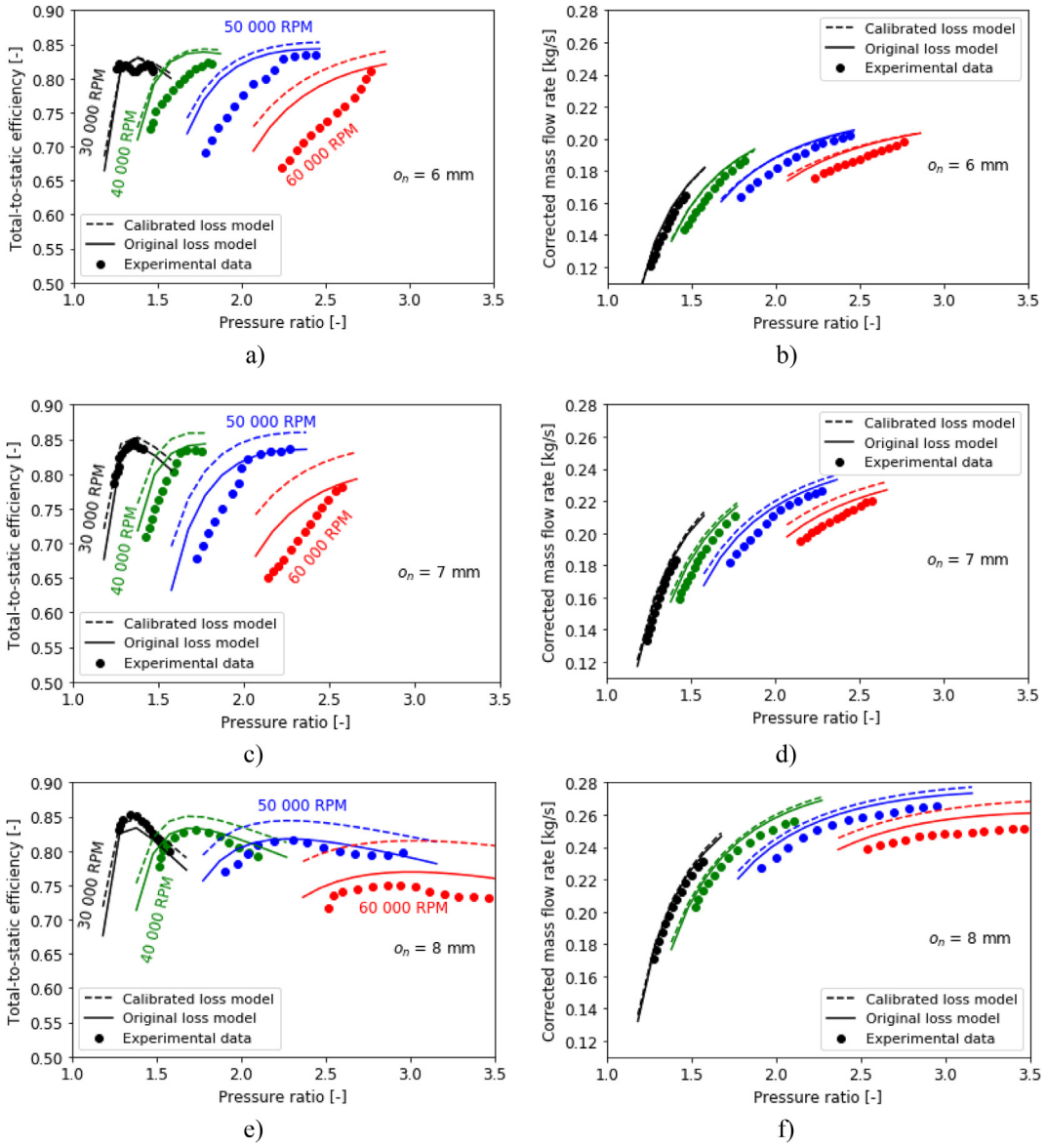

Fig. 4. Qualitative comparison between experimental data by Spence et al. [29,30] and corresponding model predictions: Total-to-static efficiency (a, c, e) and corrected mass flow rate (b, d, f).

lower bound of 0.04. These bounds were suggested by Aungier [16](p. 243) and Hu et al. [17], respectively. In addition, the inequality constraint for minimum degree of reaction, whose lower limit was proposed by Aungier [16](p. 243), was active.

The *T-s* diagrams of the ORC process and the expansion within the RIT are illustrated in Fig. 7. It can be observed that the working fluid enters the turbine at supercritical conditions and leaves as superheated vapor. In addition, the close-up view of the expansion process indicates that most of the entropy generation occurs in the rotor row and that the kinetic energy leaving the turbine is small. These results are confirmed by the loss distribution, rotor geometry, and velocity triangles illustrated in Fig. 8. More specifically, the sum of the rotor clearance, passage, and trailing edge losses leads to a reduction in the total-to-static efficiency of about 11% points, which represents 70 % of the losses. By contrast, the kinetic energy loss only penalizes the turbine total-to-static efficiency by 2.6% points, which is explained by the large flow area ($A_6/A_4 = 3.5$) and small flow angle ($\alpha_6 = 2.8°$) at the exit of the rotor. The rest of the entropy generation can be attributed to the rotor disc friction loss, the interspace loss and the losses in the nozzle ring. Notably, the nozzle operates at supersonic conditions, $Ma_3 = 1.22$, which leads to a supersonic loss that penalizes the total-to-static isentropic efficiency about one percentage point.

A one-at-a-time sensitivity analysis was performed to illustrate the sensitivity of the design efficiency to some of the assumptions used in the design problem formulation. In particular, the lower limit of the degree of reaction and values of selected parameters from Table 3 were modified up and down by 20 % of their nominal value, and a design optimization was carried out for each parameter configuration. The results from the sensitivity analysis, see Fig. 9, show that a higher design efficiency can be obtained by allowing a lower degree of reaction and that the sensitivity of the design efficiency to the number of nozzle blades and the disc clearance are negligible in comparison with the sensitivity to the degree of reaction.

One drawback of gradient-based optimization algorithms is that they may converge to a local optima close to the starting point used for the optimization. In addition, the convergence to a feasible

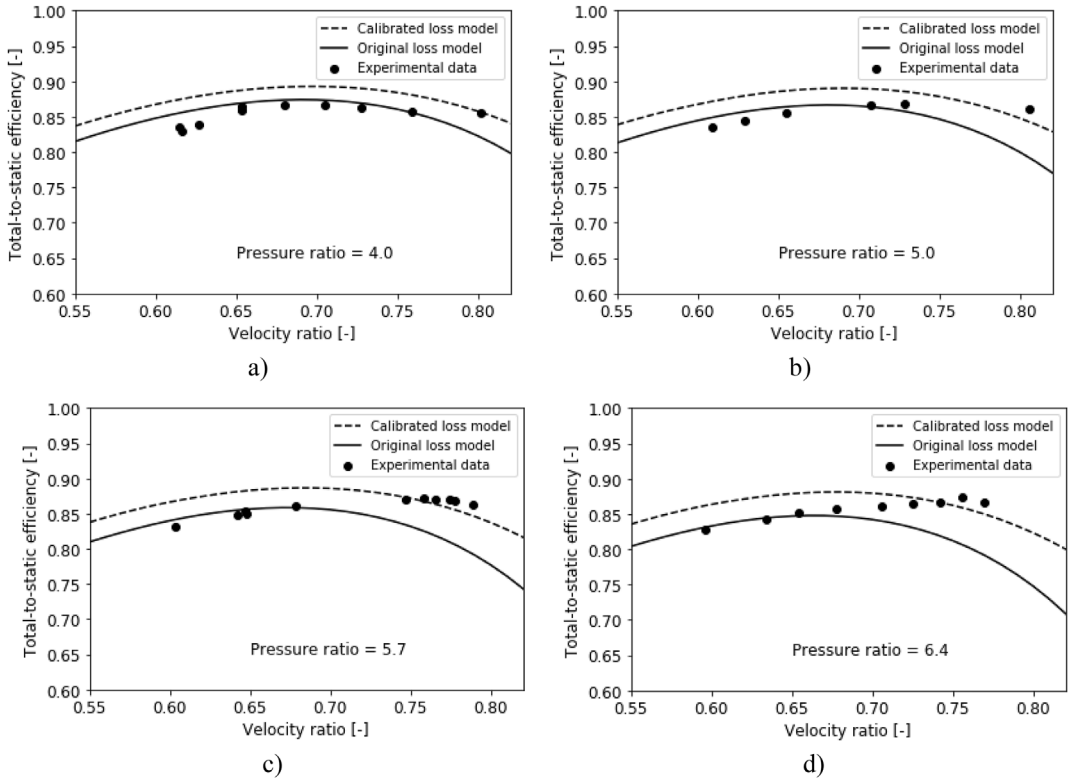

Fig. 5. Qualitative comparison between experimental data by Jones [27] and corresponding model predictions.

Table 9
Average RMS deviation between experimental data and corresponding model predictions.

Experimental data	Jones [27]		Spence et al. [29,30]	
Parameter	η_{ts}	$\dot{m}$[a]	η_{ts}	$\dot{m}$
Original loss model	3.4 %-points	2.1%	4.0 %-points	3.2%
Calibrated loss model	2.5 %-points	0.9%	5.3 %-points	3.8%

[a] Experimental data available at design point (pressure ratio of 5.78, $\nu = 0.70$) only.

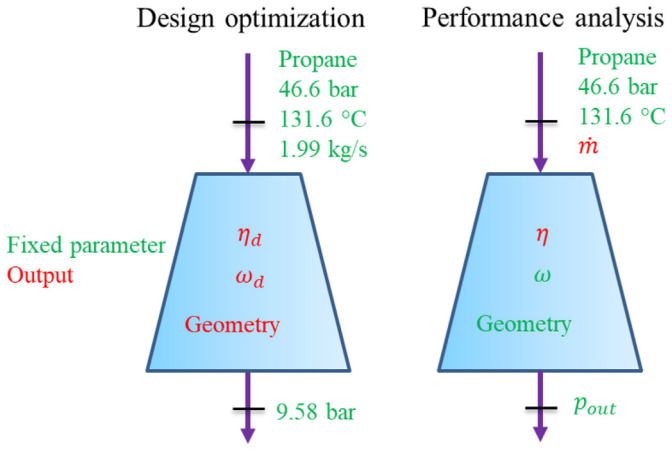

Fig. 6. Fixed operating conditions for the case study and indication of the main output parameters for the design optimization and performance analysis.

solution is only guaranteed if the objective- and the constraint functions are twice continuously differentiable. In this work, the robustness of the proposed design optimization method was assessed by carrying out 100 design optimizations starting from random initial values for the independent variables. As seen in Fig. 10(a), essentially all optimizations converged to the same solution as the optimal value of the independent variables differed by less than ± 0.06 %. The consistency in the optimization results is a strong indication that the proposed design optimization method reliably converges to the global optimum solution despite the non-smooth transition between subsonic and supersonic flow velocities in Eq. (7). The average execution time on a personal computer with an Intel Core i7-8650U CPU of 2.11 GHz was 0.97s and 76 % of the optimizations spent less than 1 s to converge, see Fig. 10(b).

4.2. Performance analysis

The off-design performance analyses were carried out using the problem formulation from Table 7 and the operating conditions indicated in Fig. 6. To this aim, the RIT geometry obtained during the design optimization, see Table 11, was provided as fixed parameters and the influence of the rotational speed, pressure ratio, and nozzle throat area on the isentropic efficiency and mass flow rate was analyzed. More specifically, the rotational speed was varied between 70 % and 110 % of its design value, the outlet pressure was varied such that the pressure ratio varied between 1.8 and 8.0, and the nozzle throat area was varied between 60 % and 120 % of its design value.

The mass flow rates predicted by the mean-line model are shown in Fig. 11. Each of the plots (a,b,c,d) corresponds to a certain nozzle throat area, whereas each colored line represents a certain rotational speed. The design condition is indicated with an “x” in the figures. It can be observed that the mass flow rate increases with the pressure ratio until choking occurs and then remains constant. Moreover, the model predicts that the pressure ratio in

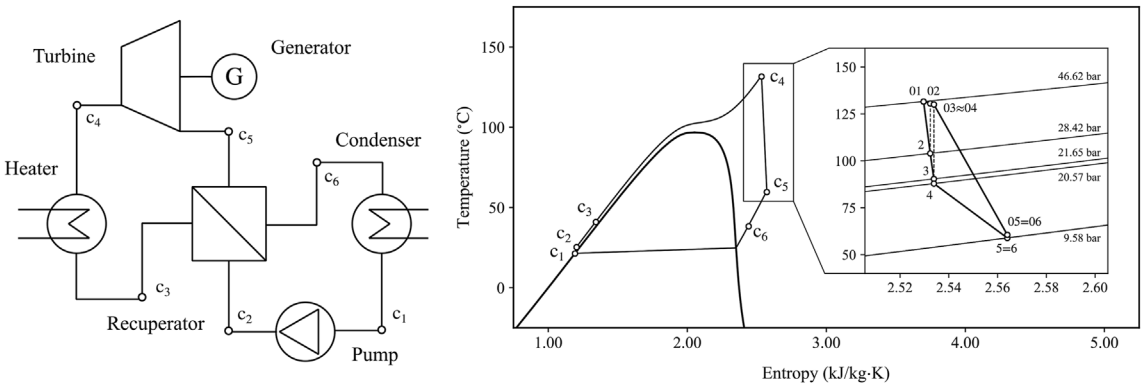

Fig. 7. Process flow diagram of the ORC considered in Ref. [40] and ***T-s*** diagrams of the ORC process and the expansion within the RIT obtained from the design optimization.

Table 10
Main results from the design optimization.

Parameter	Symbol	Value
Specific speed	ω_s	0.41
Velocity ratio	ν	0.65
Degree of reaction	R	0.45
Nozzle outlet flow angle	α_3	69.3°
Rotor outlet flow angle	α_6	2.8°
Rotor area ratio	A_6/A_4	3.5
Design rotational speed	ω_d	57 579 RPM
Design efficiency	η_d	0.841
Shaft power	$\dot{W}$	140 kW

which choking occurs is higher for higher rotational speeds. In most cases, the value of the choked mass flow rate is unaffected when the rotational speed changes. This is an indication that the flow in the nozzle is the first to choke, because in case the flow in the rotor was the first to choke, an increase in rotational speed would lead to a reduction in the mass flow rate [12] (p. 24). However, for the case when $A_2 = 1.2A_{2d}$ and $\omega = 1.1\omega_d$ the mean-line model predicts that only the rotor is choked, see Fig. 12. Indeed, as seen in Fig. 11(d), the red line is lying slightly below the other curves.

The results depicted in Fig. 11 also indicate that the nozzle throat area strongly affects the mass flow rate. Indeed, the results shown in Fig. 13 demonstrate that the mass flow rate is roughly proportional to the nozzle throat area. This trend agrees well with the experimental data of Spence et al. [30], which also suggests a relationship between mass flow rate and nozzle throat area that is roughly proportional.

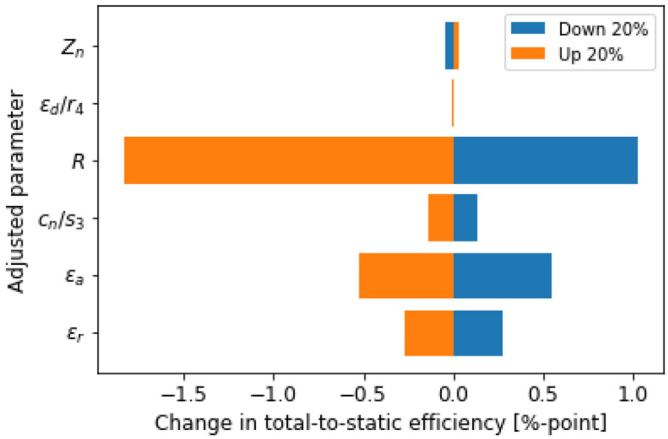

Fig. 9. Sensitivity of design efficiency to input parameters.

The total-to-static efficiencies predicted by the mean-line model are shown in Fig. 14. These results indicate that the rotational speed has a strong influence on the efficiency and that, for each rotational speed, there is a pressure ratio that maximizes the efficiency. In addition, the results illustrated in Fig. 14(c) suggest that using a rotational speed lower than the design one is advantageous when the pressure ratio is lower than the design value.

The nozzle throat area also affects the total-to-static efficiency.

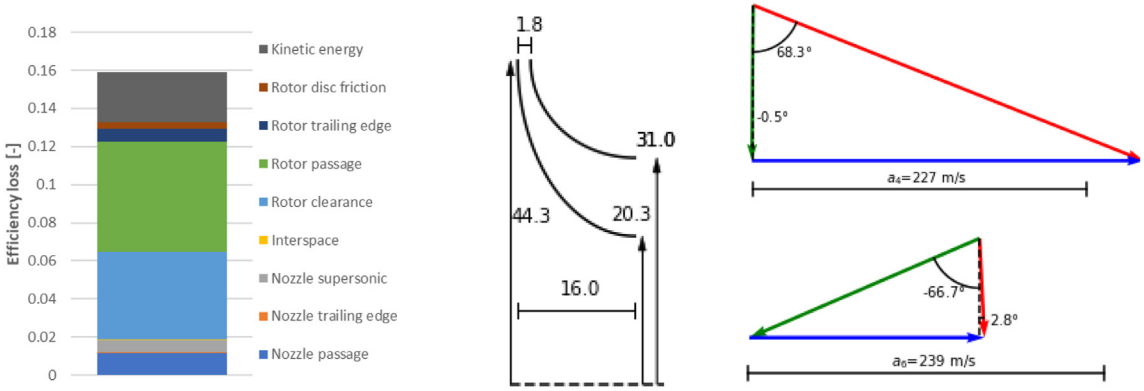

Fig. 8. Loss distribution, rotor geometry (values in mm) and rotor inlet and rotor outlet velocity triangles from the design optimization.

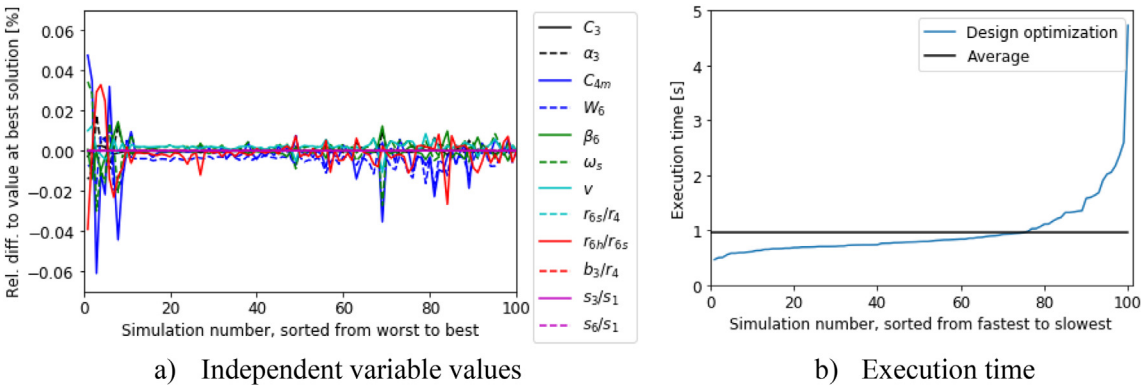

Fig. 10. Results and execution time of 100 design optimizations with random start values of the independent variables.

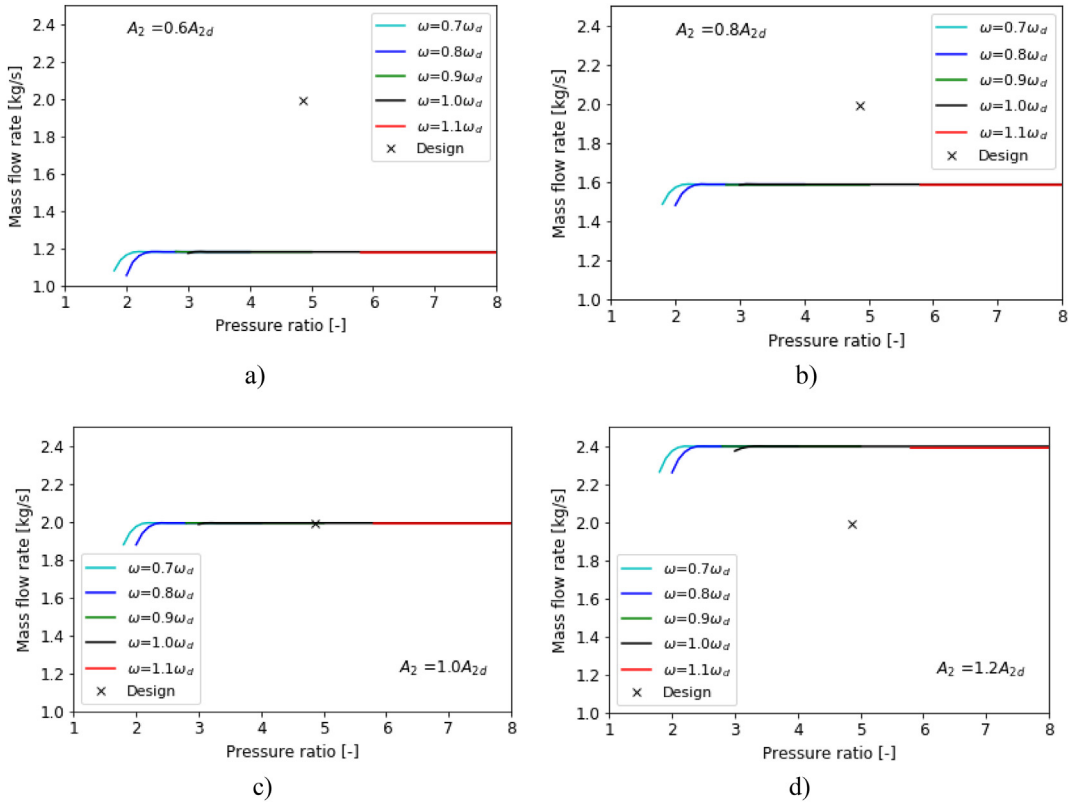

Fig. 11. Predicted mass flow rate vs. pressure ratio for different rotational speeds and nozzle throat areas.

For instance, when comparing Fig. 14(a) and (d) it is clear that, for small nozzle throat areas, the highest efficiencies occur at larger pressure ratios, while, for large nozzle throat areas, the highest efficiencies occur at the lowest pressure ratios. This trend agrees well with the experimental data concerning variable-geometry RIT measured by Spence et al. [30]. The efficiency penalization at high pressure ratios and large nozzle throat opening can be attributed to increased kinetic energy loss due to larger rotor outlet velocities [30]. Indeed, a comparison between Fig. 15(a) and (b) shows that the reduction in the total-to-static efficiency due to the kinetic energy loss for the case $A_2 = 1.2A_{2d}$ is up to five percentage points higher than that of the case $A_2 = A_{2d}$. This is not surprising because the flowrate and flow velocity leaving the rotor are larger when the nozzle throat area is increased.

The efficiency trends depicted in Fig. 14 also provide information about the pressure ratio in which the rotor chokes. In the cases when $A_2 = 0.6A_{2d}$ and $A_2 = 0.8A_{2d}$ the flow in the nozzle is the first to choke and the rotor remains unchoked. However, when $A_2 = A_{2d}$ and $A_2 = 1.2A_{2d}$ the rotor chokes at a pressure ratio about 7 and 6, respectively. The transition between unchoked and choked rotor can be observed as a kink point in the efficiency vs. pressure ratio curves in Fig. 14(c and d). After this point, all the losses upstream the rotor throat remain constant in terms of enthalpy change, see Table 4, and any additional losses are due to the rotor supersonic loss and the kinetic energy at the exit of the rotor. In fact, as illustrated by the loss distribution in Fig. 15, the predicted supersonic loss is almost negligible in comparison with the other losses and the decrease in efficiency as the pressure ratio increases can be

Table 11
RIT geometry obtained from the design optimization.

Nozzle	r_3	[mm]	45.5
	b_3	[mm]	1.77
	Z_n	[−]	20
	A_{2d}	[mm^2]	167[a]
	t_3	[mm]	0.23
	c_n	[mm]	19.4
Rotor	r_4	[mm]	44.3
	r_{6s}	[mm]	31.0
	r_{6h}	[mm]	20.3
	b_4	[mm]	1.77
	Z_r	[−]	17
	t_6	[mm]	0.89
	A_5	[mm^2]	681[a]
	L_z	[mm]	16.0
	c_r	[mm]	24.6
	ϵ_a	[mm]	0.40
	ϵ_r	[mm]	0.40
	ϵ_d	[mm]	2.21

[a] Computed such that the performance analysis at the design point and the design optimization predict equal flow angles.

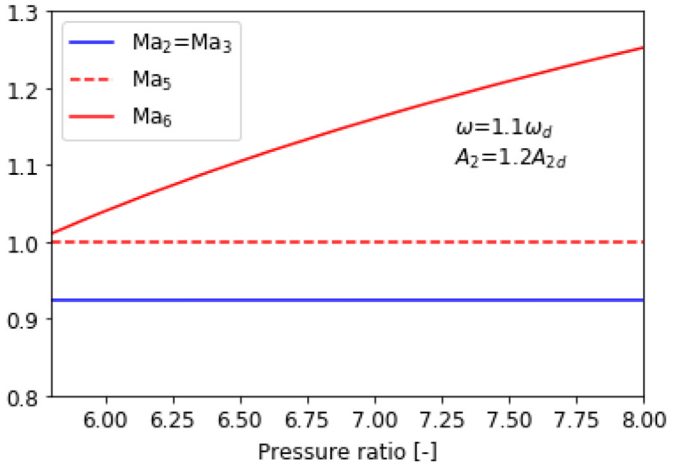

Fig. 12. Mach number at the throat and outlet of the blade rows from the performance analyses with the largest rotational speed and nozzle throat area.

attributed almost exclusively to the kinetic energy loss. The reason why some of the losses depicted in Fig. 15 (e.g., rotor passage and clearance losses) seem to decrease when the pressure ratio increases beyond the rotor choking point is that they are expressed in terms of efficiency loss, rather than as a change in enthalpy.

In order to assess the computational efficiency and robustness of the performance analysis method, all performance analyses applied the same set of start values for the independent variables. The start values of the velocity variables were equal to the corresponding optimized values from the design optimization, whereas the start values of the entropy variables were equal to 1.0. All performance analyses converged to the feasible solution at the first attempt within less than 2.5 s, see Fig. 16. This is a strong indication that the performance analysis method reliably converges to the feasible solution despite the non-smooth transition between subsonic and supersonic flow. Although the performance analysis involves fewer independent variables and constraints than the design optimization, the computational cost of the two methods is comparable. The main reason for this is that the performance analysis requires an inner iteration to compute the thermodynamic state at the throat of the blade rows when the flow conditions are supersonic. Indeed, as depicted in Fig. 16, there is a positive correlation between the execution time and the nozzle outlet Mach number.

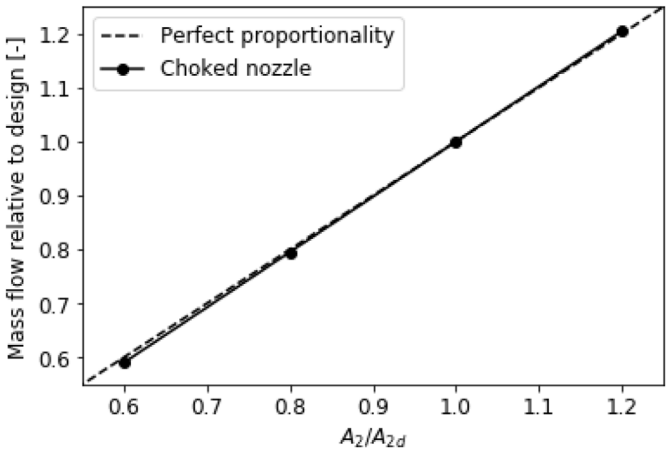

Fig. 13. Relationship between mass flow rate and nozzle throat area from the performance analyses.

5. Conclusion

This paper presented a method for the design optimization of RITs. In contrast with other design methods documented in the open literature, the proposed method was formulated following an equation-oriented approach and it uses equality constraints, rather than inner iteration loops, to close the model equations. As a result, the gradient-based algorithm used to solve the problem does not need to satisfy the model equations at each intermediate optimization iteration and the computational cost of the problem is reduced significantly. In addition, the present paper also presented a method to analyze the performance of RITs. The novelty of the proposed performance analysis method lies in the numerical treatment of choked flow conditions. Indeed, the method uses a predefined outlet pressure, rather than a predefined mass flow, to guarantee that the underlying mathematical problem has a unique solution, and it automatically detects whether the nozzle and rotor blade rows are choked. This is different from other performance analysis methods documented in the open literature, which are only suitable for subsonic flow conditions or need an a priori numerical solution strategy to identify whether any blade rows are choked.

Both the design optimization and performance analysis methods are based on a mean-line flow model and use an empirical loss model to account for the irreversibilities occurring within the turbine. The mean-line model was validated against two comprehensive sets of experimental data concerning RITs operating at different pressure ratios, rotational speeds and nozzle throat openings. It was found that the RMS deviation between the isentropic efficiency and mass flow rate predicted by the mean-line model (when using the original loss model) and the experimental measurements was less than 4% points and 3.5 %, respectively. Moreover, the mean-line model was able to correctly predict the trends of isentropic efficiency and mass flow rate as a function of the pressure ratio, rotational speed and nozzle throat area.

Finally, in order to demonstrate their capabilities, the design optimization and performance analysis methods proposed in this work were applied to design and predict the performance of the RIT of an ORC operating with propane as working fluid. The design optimization problem was solved starting from 100 random initial values of the independent variables, and the method converged to essentially the same solution. Although not formally proved, this gives a strong indication that the optimization algorithm reliably converges to the global optimum solution despite the non-smooth

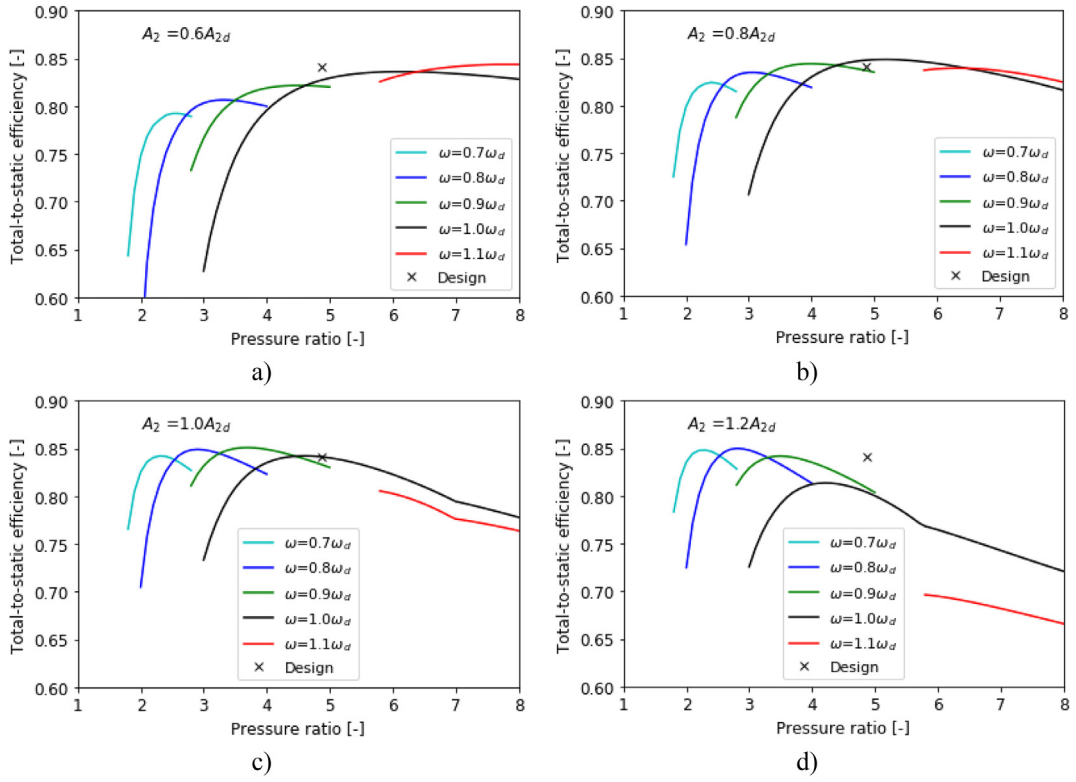

Fig. 14. Predicted efficiency vs. pressure ratio for different rotational speeds and nozzle throat areas.

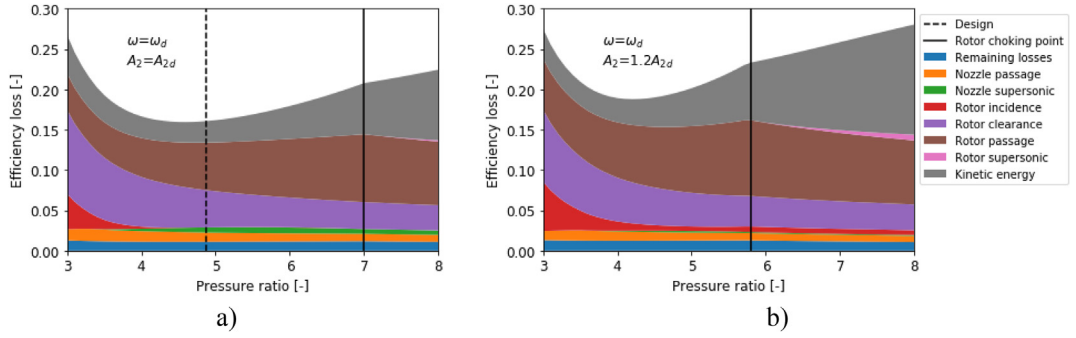

Fig. 15. Loss distribution vs. pressure ratio from some of the performance analyses.

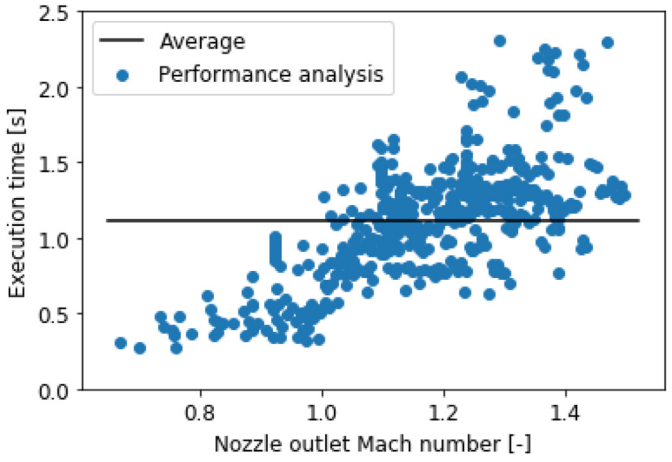

Fig. 16. Execution time vs. nozzle outlet Mach number from the performance analyses.

transition between subsonic and supersonic velocities within the mean-line model. In addition, the performance maps predicted by the performance analysis method are physically consistent and agree with general findings from experimental works available in the open literature. Notably, the performance analysis method predicts that the mass flow rate increases with the pressure ratio until choking occurs and that the corresponding mass flow rate is roughly proportional to the throat area of the choked blade row. Considering the accuracy, robustness and low computational cost of the proposed methods, they can be regarded as a powerful tool for the preliminary design and performance prediction of RITs, either as a standalone component or as part of an integrated system such as a Rankine cycle power system.

Declaration of competing interest

The authors declare that they have no known competing financial interests or personal relationships that could have

appeared to influence the work reported in this paper.

Acknowledgments

This publication has been funded by HighEFF - Centre for an Energy Efficient and Competitive Industry for the Future, an 8-years' Research Centre under the FME-scheme (Centre for Environment-friendly Energy Research, 257632). The authors gratefully acknowledge the financial support from the Research Council of Norway and user partners of HighEFF.

Appendix A. Implementation of the loss models

This Appendix describes the implementation of the loss model proposed by Meroni et al. [21]. The Reynolds number in the nozzle passage loss correlation, Eq. (9), was computed using properties at the nozzle throat and the blade height as the characteristic length, Eq. (A.1).

$$Re_2 = C_2 b_3 / \nu_2 \tag{A.1}$$

The trailing edge and supersonic loss correlations were originally proposed by Glassman [41] and Aungier [16](p. 82), respectively. However, in their original form they were expressed in terms of the total pressure loss coefficient. The factor Y_i in Eqs. (10), (11), (15) and (18) was included to convert the total-pressure-based loss correlations to enthalpy-based loss correlations. The expression for the conversion factor Y_i is given by Eq. (A.2) and it was proposed by Horlock [42].

$$Y_i = \left[1 + \frac{k_i - 1}{2} Ma_i^2\right]^{-\frac{k_i}{k_i - 1}} \tag{A.2}$$

The rotor incidence loss was implemented differently in the design optimization and the performance analysis methods. The incidence loss was disregarded in the design optimization, whereas in subsequent performance analyses the optimal rotor inlet angle, $\beta_{4,opt}$, was assigned the value of the flow angle from the design optimization, i.e. $\beta_{4,opt} = \beta_{4,d}$. This approach of forcing the minimum incidence loss to occur at the design point was proposed in Ref. [12](p. 238).

The optimal rotor inlet relative flow angle was not given in the references of the experimental data used for model validation. Therefore, a correlation given by Eq. (A.3) was applied to estimate $\beta_{4,opt}$ during the model validation.

$$\tan \beta_{4,opt} = \frac{-1.98 \tan \alpha_4}{Z_r - 1.98} \tag{A.3}$$

The rotor passage loss correlation, Eq. (14), requires the parameters L_H, D_H, c_r to be estimated. Moustapha et al. [12](p. 226) suggest to estimate the hydraulic length as the average of two quarter circles, Eq. (A.4), the hydraulic diameter as the average of the inlet and outlet hydraulic diameter, Eq. (A.5), and the rotor chord length according to Eq. (A.6). For the case of Jones' turbine [27], the value of the rotor chord was obtained from Ref. [39] rather than from Eq. (A.6).

$$L_H = \frac{\pi}{4}\left[L_z - \frac{b_4}{2} + r_4 - r_{6s} + \frac{b_6}{2}\right] \tag{A.4}$$

$$D_H = \frac{1}{2}\left[\frac{4\pi r_4 b_4}{2\pi r_4 + Z_r b_4} + \frac{2\pi\left(r_{6s}^2 - r_{6h}^2\right)}{\pi(r_{6s} + r_{6h}) + Z_r b_6}\right] \tag{A.5}$$

$$c_r = \frac{L_z}{\cos\overline{\beta}},\ \tan\overline{\beta} = \frac{1}{2}\tan\beta_{6b} \tag{A.6}$$

To the best of our knowledge, there exists no reliable correlation for the rotor deviation angle, $\delta_6 = \beta_6 - \beta_{6b}$. In addition, the use of blade metal angles is restricted to the loss model only. For these reasons the deviation angle is assumed zero unless the blade metal angle is known a priori, as was the case for the rotor in Spence et al. [29,30].

The factors K_a and K_r in the clearance loss correlation were computed by Eq. (A.7), and the derivation of these factors can be found in Ref. [12] (p. 229).

$$K_a = \frac{1 - r_{6t}/r_4}{C_{m4}},\ K_r = \frac{r_{6t}}{r_4} \cdot \frac{L_z - b_4}{C_{m5} r_6 b_6} \tag{A.7}$$

The friction coefficient, K_f, in the disc friction loss correlation, Eq. (17), is computed according to Eq. (A.8). This approach is similar to that of Meroni et al. [21] and the only difference is the value of the Reynolds number in which the transition between the laminar and the turbulent correlation occurs. As this work relies on the use of a gradient-based optimization algorithm, the transition Reynolds number of $1.58 \cdot 10^5$ was used to ensure a continuous transition between laminar and turbulent flow.

$$K_f = \begin{cases} 3.7(\varepsilon_d/r_4)^{0.1} Re_4^{-0.5},\ Re_4 = \dfrac{U_4 r_4 \rho_4}{\mu_4} < 1.58 \cdot 10^5 \\ 0.102(\varepsilon_d/r_4)^{0.1} Re_4^{-0.2}, \quad Re_4 > 1.58 \cdot 10^5 \end{cases} \tag{A.8}$$

Credit author statement

Brede A. L. Hagen: Conceptualization, Methodology, Software, Investigation, Formal analysis, Writing – original draft, Writing – review & editing, Visualization Roberto Agromayor: Methodology, Writing – review & editing, Visualization Petter Nekså; Writing – review & editing, Supervision.

References

[1] Macchi E. Theoretical basis of the organic rankine cycle. In: Macchi E, Astolfi M, editors. Organic Rankine cycle (ORC) power systems: Technologies and applications. Woodhead Publishing; 2017. p. 3–24.

[2] Tian H, Shu GQ. Organic Rankine Cycle systems for large-scale waste heat recovery to produce electricity. In: Macchi E, Astolfi M, editors. Organic Rankine cycle (ORC) power systems: Technologies and applications. Woodhead Publishing; 2017. p. 613–36.

[3] Guercio A, Bini R. Biomass-fired Organic Rankine Cycle combined heat and power systems. In: Macchi E, Astolfi M, editors. Organic Rankine cycle (ORC) power systems: Technologies and applications. Woodhead Publishing; 2017. p. 527–67.

[4] Orosz M, Dickes R. Solar thermal powered organic rankine cycles. In: Macchi E, Astolfi M, editors. Organic Rankine cycle (ORC) power systems: Technologies and applications. Woodhead Publishing; 2017. p. 569–612.

[5] Spadacini C, Xodo LG, Quaia M. Geothermal energy exploitation with organic rankine cycle technologies. In: Macchi E, Astolfi M, editors. Organic Rankine cycle (ORC) power systems: Technologies and applications. Woodhead Publishing; 2017. p. 473–525.

[6] Tchanche BF, Pétrissans M, Papadakis G. Heat resources and organic Rankine cycle machines. Renew Sustain Energy Rev 2014;39:1185–99.

[7] Colonna P, et al. Organic rankine cycle power systems: from the concept to current technology, applications, and an outlook to the future. J Eng Gas Turbines Power 2015;137(10):1–19.

[8] Capra F, Martelli E. Numerical optimization of combined heat and power Organic Rankine Cycles – Part B: simultaneous design & part-load optimization. Energy Oct. 2015;90:329–43.

[9] Song J, Gu C, Ren X. Influence of the radial-inflow turbine efficiency prediction on the design and analysis of the Organic Rankine Cycle (ORC) system. Energy Convers Manag Sep. 2016;123:308–16.

[10] Chatzopoulou MA, Simpson M, Sapin P, Markides CN. Off-design optimisation

of organic Rankine cycle (ORC) engines with piston expanders for medium-scale combined heat and power applications. Appl Energy Mar. 2019;238:1211–36.
[11] Bahamonde S, Pini M, De Servi C, Rubino A, Colonna P. Method for the preliminary fluid dynamic design of high-temperature mini-organic rankine cycle turbines. J Eng Gas Turbines Power 2017;139(8):1–14.
[12] Moustapha H, Zelesky MF, Baines NC, Japikse D. Axial and radial turbines. Vermont, USA: Concepts NREC; 2003.
[13] Valdimarsson P. "Radial inflow turbines for organic rankine cycle systems. In: Macchi E, Astolfi M, editors. Organic Rankine cycle (ORC) power systems: Technologies and applications. Woodhead Publishing; 2017. p. 321–34.
[14] Schuster S, Markides CN, White AJ. Design and off-design optimisation of an organic Rankine cycle (ORC) system with an integrated radial turbine model. Appl Therm Eng Jun. 2020;174:115192.
[15] Li S, Krivitzky EM, Qiu X. Meanline modeling of a radial-inflow turbine nozzle with supersonic expansion. In: Proceedings of the ASME Turbo Expo:Turbomachinery Technical Conference and Exposition; 2016. p. 1–14.
[16] Aungier RH. Turbine aerodynamics: axial-flow and radial-inflow turbine design and analysis. New York: ASME Press; 2005.
[17] Hu D, Li S, Zheng Y, Wang J, Dai Y. Preliminary design and off-design performance analysis of an Organic Rankine Cycle for geothermal sources. Energy Convers Manag May 2015;96:175–87.
[18] Demierre J, Rubino A, Schiffmann J. Modeling and experimental investigation of an oil-free microcompressor-turbine unit for an organic rankine cycle driven heat pump. J Eng Gas Turbines Power 2015;137(3):1–10.
[19] Song J, Gu C, Ren X. Parametric design and off-design analysis of organic Rankine cycle (ORC) system. Energy Convers Manag Mar. 2016;112:157–65.
[20] Da Lio L, Manente G, Lazzaretto A. A mean-line model to predict the design efficiency of radial inflow turbines in organic Rankine cycle (ORC) systems. Appl Energy Nov. 2017;205:187–209.
[21] Meroni A, Robertson M, Martinez-Botas R, Haglind F. A methodology for the preliminary design and performance prediction of high-pressure ratio radial-inflow turbines. Energy Sep. 2018;164:1062–78.
[22] Alshammari F, Karvountzis-Kontakiotis A, Pesiridis A, Giannakakis P. Off-design performance prediction of radial turbines operating with ideal and real working fluids. Energy Convers Manag Sep. 2018;171:1430–9.
[23] Du Y, Chen K, Dai Y. A study of the optimal control approach for a Kalina cycle system using a radial-inflow turbine with variable nozzles at off-design conditions. Appl Therm Eng Feb. 2019;149:1008–22.
[24] Liu C, Gao T. Off-design performance analysis of basic ORC, ORC using zeotropic mixtures and composition-adjustable ORC under optimal control strategy. Energy Mar. 2019;171:95–108.
[25] Zhou K, Wang J, Xia J, Guo Y, Zhao P, Dai Y. Design and performance analysis of a supercritical CO2 radial inflow turbine. Appl Therm Eng 2020;167(December 2019):114757.
[26] Lee S, Yaganegi G, Mee DJ, Guan Z, Gurgenci H. Part-load performance prediction model for supercritical CO2 radial inflow turbines. Energy Convers Manag 2021;235(March):113964.
[27] Jones AC. Design and test of a small, high pressure ratio radial turbine. J Turbomach 1996;118(2):362–70.
[28] Hagen BAL, Cavo M, Andresen T, Nekså P. Gradient based design optimization of a radial inflow turbine. In: IIR Rankine 2020 Conference; 2020.
[29] Spence SW, Artt DW. Experimental performance evaluation of a 99.0 mm radial in flow nozzled turbine with different stator throat areas. In: Proceedings of the Institution of Mechanical Engineers, Part A: Journal of power and energy, vol. 211; 1997. p. 477–88.
[30] Spence SWT, Doran WJ, Artt DW. "Experimental performance evaluation of a 99.0 mm radial inflow nozzled turbine at larger stator-rotor throat area ratios. Proc Inst Mech Eng Part A J Power Energy 1999;213(3):205–18.
[31] Perdichizzi A, Lozza G. Design criteria and efficiency prediction for radial inflow turbines. In: Gas turbine Conference and Exhibition; 1987. p. 1–9.
[32] Rohlik HE. Analytical Determination of radial inflow turbine design geometry for maximum efficiency. 1968. Washington D.C.
[33] Rodgers C. A cycle analysis technique for small gas turbines. In: Proceedings of the Institution of Mechanical Engineers. vol. 183; 1969. p. 37–49. 14.
[34] Dixon SL, Hall CA. Fluid Mechanics and thermodynamics of Turbomachinery. seventh ed. Oxford, UK: Butterworth-Heinemann; 2014.
[35] Lemmon EW, Bell IH, Huber ML, McLinden MO. NIST standard reference Database 23: reference fluid thermodynamic and Transport properties-REFPROP, Version 10.0, National Institute of standards and technology. 2018.
[36] Schittkowski K. NLPQL: a FORTRAN subroutine solving constrained nonlinear programming problems. Ann Oper Res 1985;5(1–4):485–500.
[37] Saravanamutto HIH, Rogers GFC, Cohen H, Straznicky PV. Gas turbine theory. sixth ed. Pearson Education; 2009.
[38] GNU operating system." [Online]. Available: www.gnu.org.
[39] Sauret E. Open design of high pressure ratio radial-inflow turbine for academic validation. In: Proceedings of the ASME International Mechanical engineering Congress and Exposition, vol. 7; 2012. p. 3183–97.
[40] Hagen BAL, Nikolaisen M, Andresen T. A novel methodology for Rankine cycle analysis with generic heat exchanger models. Appl Therm Eng Jan. 2020;165:114566.
[41] Glassman AJ. Enhanced analysis and users manual for radial-inflow turbine conceptual design code RTD. NASA Contractor Report 195454, no. Lewis Research Center; 1995.
[42] Horlock JH. Losses and efficiencies in axial-flow turbines. Int J Mech Sci 1960;2(1–2):48–75.